

See discussions, stats, and author profiles for this publication at: <https://www.researchgate.net/publication/233962423>

Growth and Morphology of Ceria on Ruthenium (0001)

ARTICLE in THE JOURNAL OF PHYSICAL CHEMISTRY C · DECEMBER 2012

Impact Factor: 4.77 · DOI: 10.1021/jp3081782

CITATIONS

21

READS

63

6 AUTHORS, INCLUDING:



Sanjaya D. Senanayake

Brookhaven National Laboratory

109 PUBLICATIONS 1,794 CITATIONS

SEE PROFILE



Jerzy T. Sadowski

Brookhaven National Laboratory

112 PUBLICATIONS 1,640 CITATIONS

SEE PROFILE



J. Falta

Universität Bremen

196 PUBLICATIONS 1,540 CITATIONS

SEE PROFILE



Jan Ingo Flege

Universität Bremen

92 PUBLICATIONS 1,626 CITATIONS

SEE PROFILE

Growth and Morphology of Ceria on Ruthenium (0001)

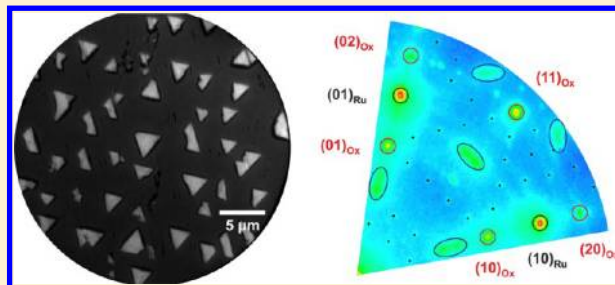
B. Kaemena,[†] S. D. Senanayake,[‡] A. Meyer,[†] J. T. Sadowski,[§] J. Falta,[†] and J. I. Flege^{*,†}

[†]Institute of Solid State Physics, University of Bremen, Otto-Hahn-Allee 1, 28359 Bremen, Germany

[‡]Chemistry Department, Brookhaven National Laboratory, Upton, New York 11973, United States

[§]Center for Functional Nanomaterials, Brookhaven National Laboratory, Upton, New York 11973, United States

ABSTRACT: Cerium oxide plays an important role in catalysis due to its prominent ability to store, transport, and release oxygen. Inverse model catalysts have attracted strong interest since their study promises a better understanding of the basic fundamentals of catalysis, but still a lot remains unknown about their structure and morphology. Here, we present an extensive growth and morphology study of the inverse catalyst model system ceria on Ru(0001) by applying spectroscopic photoemission and low-energy electron microscopy. Triangular three-dimensional islands of ceria were grown by depositing cerium metal in an oxygen ambient. We were able to control the island size, nucleation density, and oxidation state by choosing appropriate growth conditions. For highly oxidized ceria, we observe a commensurate (7×7) diffraction pattern, demonstrating that the oxide–metal interface is well-ordered. Furthermore, two distinct types of cerium oxide rotational domains are identified, whose quantity, average azimuthal alignment, and distribution with respect to the principle directions of the substrate lattice strongly depend on the growth conditions. Together, these findings are expected to have a high impact on the catalytic behavior of the model system.



INTRODUCTION

Cerium oxide is currently under extensive investigation due to its intriguing physical and chemical properties arising from the existence of different oxidation states associated with the unfilled 4f electron shell, which make it a promising material for numerous applications. Because of its prominent ability to store and release oxygen, the use of ceria is attractive for catalysis¹ and solid oxide fuel cells.² Owing to its high dielectric constant, other fields of application include the use in microelectronics,^{3–5} for example, as a replacement for the SiO₂ gate oxide and its successors or as a buffer layer for the silicon-on-insulator technology.

The role of ceria in catalysis is well-documented,¹ and it has become of importance as an energy critical material under continuous investigation in numerous applications related to H₂ production in the water gas shift reaction (WGS),⁶ solar hydrogen production,⁷ mediation of noxious automotive exhausts (NO_x and CO),⁸ and fuel cell applications.⁹ So far, ceria inverse model systems have been realized by reactive epitaxy of cerium metal in oxygen ambient on Au(111),¹⁰ Cu(111),¹¹ Ni(111),¹² Re(0001),¹³ Rh(111),¹⁴ Ru(0001),^{12,15,16} Pd(111),¹⁷ and Pt(111).¹⁸ These model systems have been successfully employed to understand complex “real” catalyst systems where active sites and the nature of the reaction pathways are deconstructed through systematic experiments^{19–24} with increasing degrees of complexity; from metals to oxides to supported metal oxides to inverse catalysts. However, a lot remains unknown about the structure of these model systems, especially the growth mechanism that leads to the creation of sites necessary for chemical activity and selectivity: termed the active sites. These have frequently been associated with

undercoordinated sites, which may be found, for example, at step edges. Moreover, recent studies by Nilius et al.²⁵ suggest that even the type of step edges of ceria islands could have a high influence on the chemical activity of ceria.

Only few of the investigations concerning the growth and structure of ceria inverse model catalysts have been devoted to microscopic investigations, for example, using scanning tunneling microscopy (STM)^{26,27} and atomic force microscopy (AFM),²⁸ but none have utilized low-energy and photoemission electron microscopy (LEEM/PEEM), which allows in situ probing of the surface structure and reactions at nanometer resolution and video rates. Here, we present an extensive study of cerium oxide structure and morphology on Ru(0001) depending on substrate temperature and oxygen partial pressure during deposition. Specifically, we will show that cerium oxide forms a commensurate superstructure and that the step edge orientations sensitively depend on the growth conditions and the oxidation state. Furthermore, we note that this study significantly extends the investigated temperature range up to 1000 °C, providing in situ, dynamic access to the structure and dynamical behavior of cerium oxide during high-temperature redox processes.

EXPERIMENTAL SECTION

The measurements were performed in a commercial Elmitec SPE-LEEM (spectroscopic photoemission and low-energy electron microscope) installed at beamline USUA of the

Received: August 16, 2012

Revised: November 30, 2012

Published: December 4, 2012



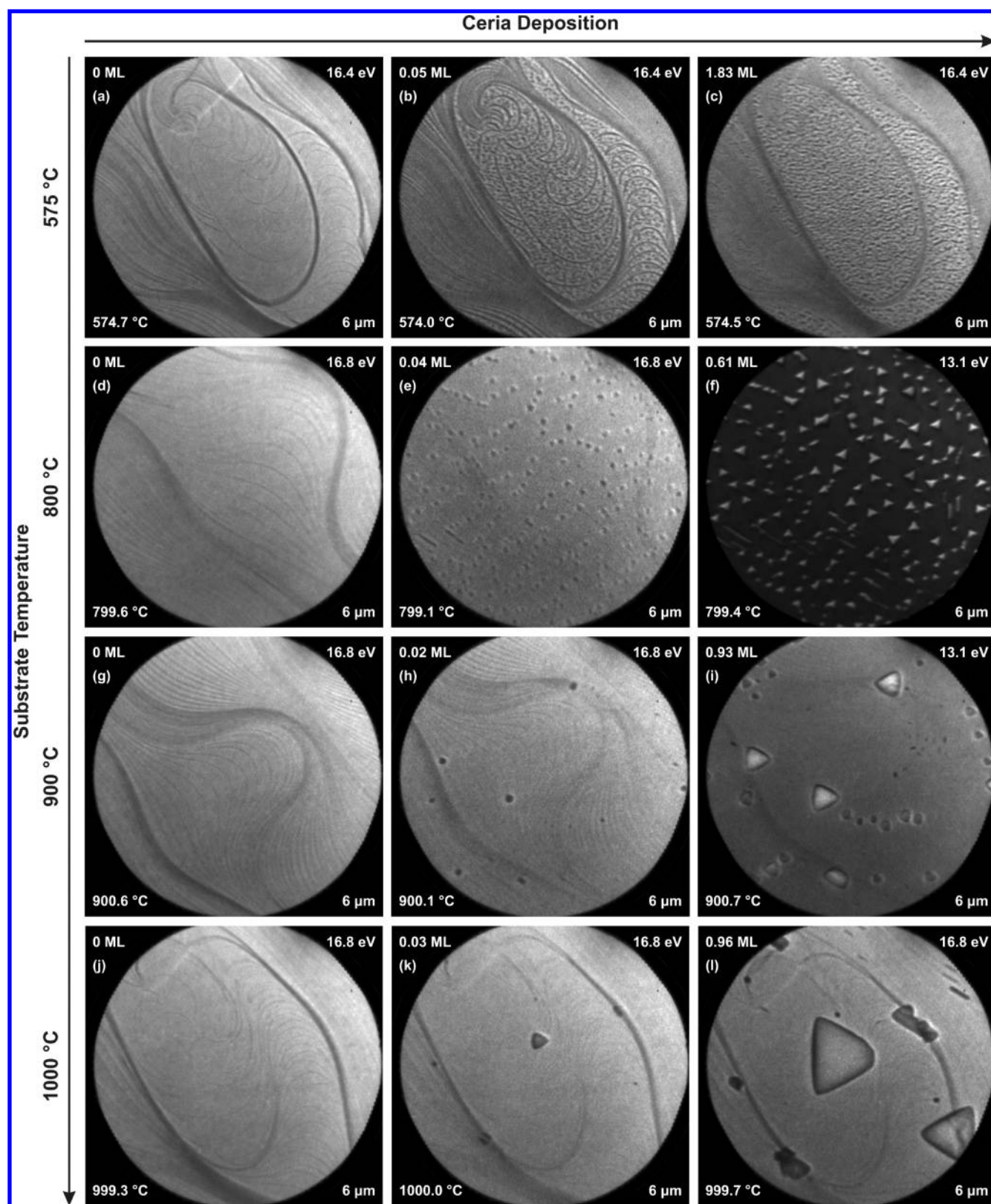


Figure 1. Growth of ceria on Ru(0001) at different substrate temperatures and stages of growth (increasing deposited amount of ceria). From left to right: advancing stage of growth. From top to bottom: increasing substrate temperature. The ceria island size increases with substrate temperature while the ceria island density decreases. The different contrast in panels (f) and (i) compared to the other panels is due to a different electron kinetic energy.

National Synchrotron Light Source (NSLS) at Brookhaven National Laboratory (BNL), Upton, New York, allowing in situ microscopy with low-energy electrons that are provided by the microscope's electron gun or with photoelectrons that are

excited by synchrotron radiation.²⁹ The instrument offers two different ultra-high-vacuum (UHV) chambers. The sample preparation chamber and the main chamber have base pressures of 5×10^{-10} and 1×10^{-10} Torr, respectively. The sample

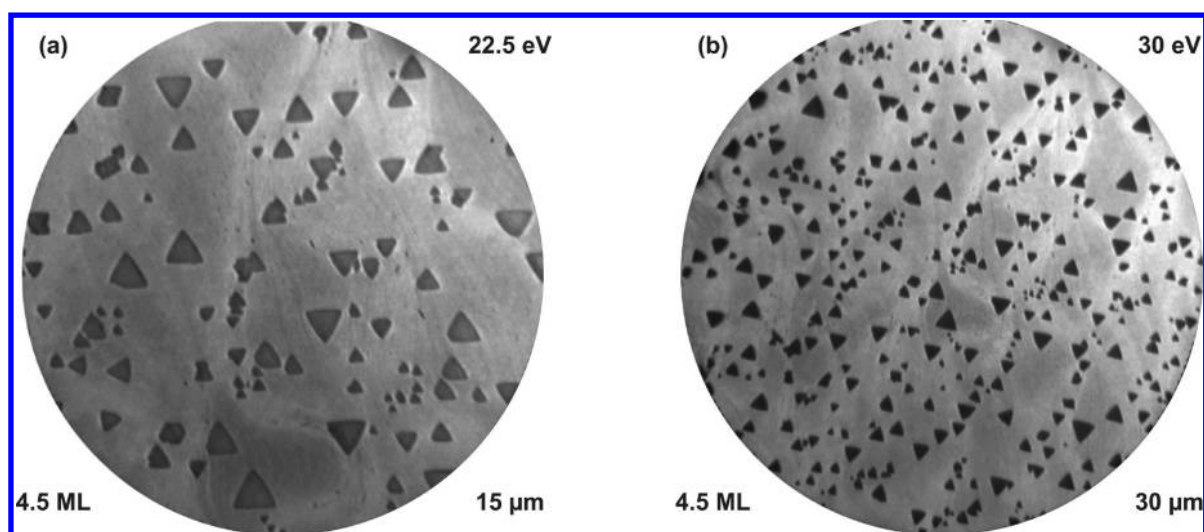


Figure 2. Different fields of view of ceria grown on Ru(0001) at a 900 °C substrate temperature and an oxygen partial pressure of 5×10^{-7} Torr showing the nucleation behavior of the islands on substrate terraces and step bunches. (a) FOV = 15 μm and (b) FOV = 30 μm . Ceria islands with an almost perfect triangular shape preferentially develop on substrate terraces while the islands density is strongly increased at step bunches. The different contrast in the panels is due to different electron kinetic energies during image acquisition.

preparation chamber is used for degassing, sputtering, and heating samples, while the main chamber is used for the ceria in situ deposition on the ruthenium substrate and performing the actual measurements.

Atomic force microscopy (AFM) measurements were carried out at the Center of Functional Nanomaterials (CFN) at Brookhaven National Laboratory with a commercial Veeco Multimode V scanning probe microscope under ambient conditions.

The substrate used for the experiments is a commercially purchased, polished Ru(0001) single crystal (Mateck) with a nominal orientation better than 0.1° . The crystal was initially cleaned ex situ by repeated cycles of oxidation and high-temperature annealing under an Ar gas flow before it was introduced into the SPE-LEEM microscope, where it was degassed at 600 °C for at least 12 h in the preparation chamber. To further remove contaminations and to obtain larger terraces on the Ru(0001) surface, the crystal was repeatedly oxidized and flashed to over 1500 °C in the main chamber following a well-established procedure.³⁰

Prior to ceria growth, the Ru(0001) surface was analyzed in low-energy electron diffraction (LEED) and LEEM mode. Only if very sharp Ru(0001) diffraction spots and no surface contamination were visible, the samples were prepared. Ceria was then grown in situ under UHV conditions by reactive molecular beam epitaxy (MBE) at substrate temperatures between 360 and 1000 °C using an electron beam evaporator to evaporate metallic Ce from a molybdenum crucible under preset oxygen background pressures between 1×10^{-8} and 5×10^{-7} Torr with a deposition rate of approximately 0.15 ML/min. Here, we define a ceria monolayer (ML) as the thickness of a O–Ce–O trilayer of the (111)-oriented fluorite structure corresponding to a thickness of 3.12 Å. High-temperature postdeposition annealing in oxygen or vacuum was only applied to the grown ceria films when explicitly mentioned.

All substrate temperatures were measured by a standard W-Re thermocouple, which was spot-welded to the sample holder very close to the substrate.

Between different sample preparations, the crystal was flashed to over 1500 °C to remove the ceria film and then further cleaned

by repeated cycles of oxidation and high-temperature annealing. The surface quality and contamination was again checked by LEED and LEEM.

The LEEM, LEED, and X-ray photoemission electron microscopy (XPEEM) investigations were conducted in situ at sample temperatures between room temperature and 1000 °C during or after evaporation of ceria. The AFM measurements were performed ex situ. The data were analyzed using the open source software package Gxsm developed by P. Zahl.³¹

RESULTS AND DISCUSSION

Growth Mode and Characteristics. In the following, we will discuss the growth mode and characteristics of highly oxidized ceria on ruthenium (0001). To ensure an oxidation state of $\text{CeO}_{2-\delta}$ with δ close to zero, ceria was grown under oxygen partial pressures in the regime of 2×10^{-7} to 5×10^{-7} Torr.

Figure 1 shows LEEM images recorded during the growth of ceria on Ru(0001) at different stages of growth (amount of deposited ceria) and varying substrate temperatures. For every temperature, a sequence of three images is shown (575 °C, (a)–(c); 800 °C, (d)–(f); 900 °C, (g)–(i); 1000 °C, (j)–(l)). The first image of each sequence shows the ruthenium substrate with oxygen backfilling already applied, but with the shutter of the cerium evaporator still closed. At this stage, only atomic steps (thin dark lines) and step bunches (broad dark lines) are visible, with atomically flat terraces in between. The second image of each sequence shows the ceria growth at very low coverages of 0.02–0.05 ML, while the third image illustrates characteristic images for the advanced growth at coverages between 0.61 and 1.83 ML. We note that the different contrast observed in Figure 1f,i compared to the other panels is due to a different electron kinetic energy of $E_{\text{kin}} = 13.1$ eV during image acquisition instead of $E_{\text{kin}} = 16.4$ eV. For these deposits, individual islands have already nucleated (dark or bright features).

The growth sequence at 575 °C suggests the development of a closed ceria film with progressing ceria coverage. The sequences at higher deposition temperature, however, reveal the formation of ceria islands with a temperature-dependent ceria island density and ceria island size. The island size increases with temperature while the island density decreases, resulting in ceria islands with

an almost perfect triangular shape, as shown in Figure 1l. Therefore, we conclude that the ceria film grown at a temperature of 575 °C (Figure 1c) also consists of very small ceria islands with a huge density that cannot be resolved in LEEM. At this point, we also note that, for all preparation conditions applied, we never observe the formation of ruthenium oxide species, in agreement with the extremely low dissociative sticking coefficient observed for molecular oxygen at oxygen-submonolayer phases.³²

By comparing the second and third images of each deposition temperature growth series, we observe that the density of nucleation centers is mainly determined by the growth temperature and that the nuclei density does not depend on the deposited amount of ceria. The nucleation centers are formed at a very early stage of growth with coverages in the regime of a few percent of a monolayer, as shown in the second image of each growth sequence. The additionally deposited amount of ceria only increases the size of the ceria islands and does not change the nuclei density. This indicates an Arrhenius-like behavior, which will be further discussed at the end of this section. Furthermore, we infer a single crystalline island growth since each island develops from a single nucleation center, as evidenced by real-time LEEM video sequences recorded during deposition (not shown).

In the following, we investigate the influence of substrate surface morphology on ceria island size and island density. For this purpose, ceria grown at 900 °C was examined under different fields of view (FOV) after the deposition of 4.5 ML of ceria. Figure 2 illustrates the following correlation. At the same growth conditions, ceria grown on Ru(0001) exhibits a decreased island size and an increased island density at substrate step bunches, while it preferentially develops a perfect triangular shape on substrate terraces. For the electron kinetic energies used for LEEM image acquisition, step bunches appear brighter³³ than extended terraces due to preferential oxygen uptake at highly stepped regions, concomitant with early nucleation³⁴ of the (1 × 1)-O adlayer phase from the (2 × 1)-O saturation coverage at near-UHV pressures. Hence, in addition to the deposition temperature, both the island nucleation density and their shape are substantially determined by the surface morphology of the substrate.

For an in-depth look at the island height and shape, we employed ex situ atomic force microscopy (AFM). Figure 3 shows an image with the respective linescans for a sample grown at an 800 °C substrate temperature and an oxygen partial pressure of 5×10^{-7} Torr with a ceria coverage of 1 ML. Almost all islands seen in the AFM image show a perfect triangular shape. The visible dark spots are attributed to contamination arising from exposing the sample to ambient conditions. The linescans in Figure 3b show approximately 3 nm tall islands with very sharp ceria island edges. The islands also exhibit large terraces and step edges. Also, it appears that the step edges on the ceria islands are significantly influenced by the step edges of the substrate, as deduced from complementary LEEM images that were recorded in a slightly out-of-focus condition. By applying this imaging condition for several electron kinetic energies, it is possible to correlate the occurrence of the ceria step edges with the substrate step edges. A detailed analysis of the shape of the ceria islands yields that the triangles are not perfectly equilateral. Two sides of the triangle have the same lengths; that is, they are isosceles, while the remaining side is shorter. The corresponding angles amount to $66 \pm 1^\circ$ and $54 \pm 1^\circ$.

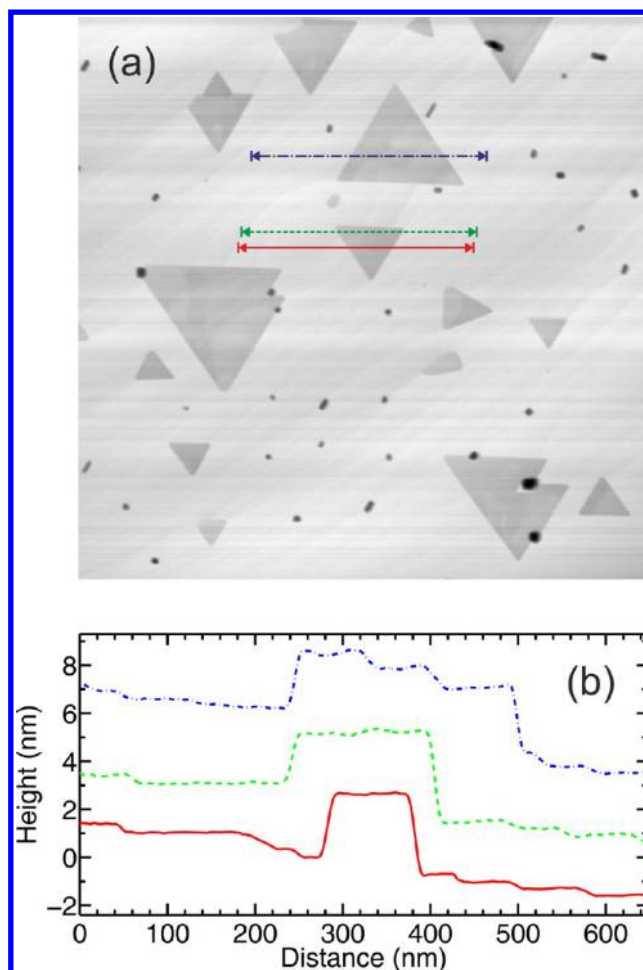


Figure 3. (a) $1.5 \times 1.5 \mu\text{m}^2$ ex situ AFM image of fully oxidized ceria islands on Ru(0001) with a coverage of 1 ML grown at an 800 °C substrate temperature and an oxygen partial pressure of 5×10^{-7} Torr. (b) Respective linescans showing approximately 3 nm tall ceria islands with sharp edges and the terraces and steps of the Ru(0001) substrate surface. For presentation purposes, panels (a) and (b) exhibit different background subtractions and the linescans in panel (b) are shifted in the vertical direction.

From the Arrhenius-like dependency between island nucleation density and growth temperature, we find an effective activation energy of $E_A = 2.03 \pm 0.08$ eV, as derived from Figure 4. In principle, it should be possible to derive the diffusion barrier height E_d from the activation energy by applying the nucleation theory by Venables et al.³⁵ However, since there are too many unknown parameters for the diffusion and attachment of ceria on ruthenium, including the precise knowledge of the diffusing species, at this point, it is too speculative to quantitatively derive a diffusion barrier height from nucleation theory.

In summary, we conclude from the in situ LEEM and ex situ AFM investigations that ceria forms triangular 3D islands on Ru(0001) adhering to a Volmer–Weber growth mode.³⁶ Depending on substrate temperature and substrate morphology, the island size and nucleation density are changed in an Arrhenius-like fashion. For high temperatures, almost perfectly triangular, nonequilateral ceria islands preferentially develop on substrate terraces. This finding is, therefore, at variance with the results published for other inverse catalyst model systems, for example, ceria on Pt(111)^{18,37} or ceria on Rh(111),^{14,38} where

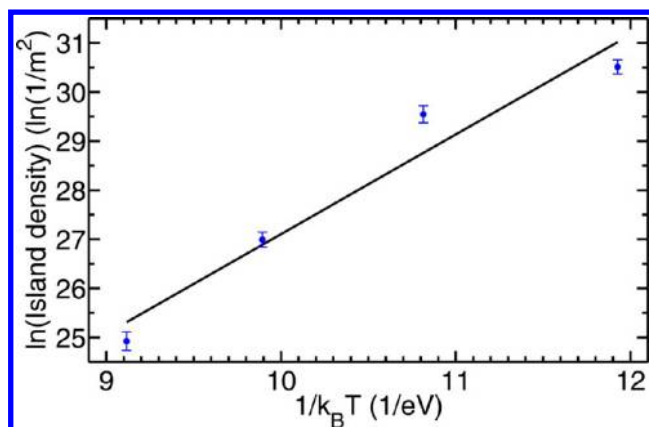


Figure 4. Ceria island density as a function of growth temperature in the range of 700–1000 °C showing an Arrhenius-like behavior with an activation energy of $E_A = 2.03 \pm 0.08$ eV. The island densities were derived from LEEM images of samples grown under oxygen partial pressures in the regime of 2×10^{-7} to 5×10^{-7} Torr with a ceria coverage between 1.5 and 4.5 ML.

hexagonally shaped islands have been reported, albeit at lower growth temperatures.

Ceria Oxidation State. To study the influence of the growth conditions on the ceria oxidation state, we applied XPEEM using the Ce 4d core level at $h\nu = 165$ eV incident photon energy. While the analysis of the detailed Ce 4d core-level structure, which essentially results from interatomic hybridization and strong intraatomic multiplet coupling effects between the Ce 4d and 4f states,³⁹ is beyond the scope of this paper, it is still possible to derive the oxidation state of ceria by comparing the peak intensities of the peaks W''' and X''' with the intensity of the remaining spectrum.⁴⁰ Figure 5a shows the Ce 4d spectrum after background subtraction of inelastically scattered electrons of a sample grown at 850 °C and an oxygen partial pressure of 5×10^{-7} Torr. We note that, because of the typically lower resolution of the photoelectron spectra acquired in XPEEM mode as compared to available high-resolution X-ray photoelectron spectra,⁴¹ the peaks shown here generally appear somewhat broader. From the relative intensity distribution of the peaks W'''

and X''' compared to the intensity of the peaks A, B, and C, we conclude that ceria is nearly fully oxidized at these growth conditions. The situation changes if we apply less oxygen partial pressure during growth. Figure 5b shows the Ce 4d spectrum, again after background subtraction, of a sample grown at 360 °C and an oxygen partial pressure of 1×10^{-8} Torr. Here, we find that the peaks W''' and X''' contribute far less intensity to the spectrum illustrating a lower oxidation state of ceria.

In principle, the oxidation state should not only depend on the oxygen partial pressure applied during growth but also on the deposition temperature, because ceria grown on metal substrates and sequentially annealed in UHV at high temperatures is found to be strongly reduced.^{13,42} However, here, we demonstrate a very high oxidation state even for an 850 °C deposition temperature, which means that CeO_2 can readily be stabilized at high deposition temperatures by oxygen partial pressures in the 5×10^{-7} Torr regime. By applying resonant photoelectron emission (RPES) measurements of the ceria valence band⁴³ (data not shown), we find that ceria grown at 430 °C can already be fully oxidized by oxygen partial pressures of 1×10^{-7} Torr.

From the above findings, we conclude that ceria grown at a deposition rate of approximately 0.15 ML/min used in our experiment and an oxygen partial pressure of 1×10^{-8} Torr during growth is partially reduced, whereas an oxygen partial pressure of 5×10^{-7} Torr leads to highly oxidized ceria even for very high temperatures, such as 850 °C. This means that, during growth at high temperatures, the same high Ce^{4+} oxidation state may be obtained simply by increasing the oxygen partial pressure, with the beneficial evolution of large, flat, single-crystalline cerium oxide, avoiding the twist mosaicity of ceria films at lower substrate temperature, which will be discussed in the following.

Lateral Surface Structure and Film Registry. LEED is perfectly suited for investigating the lateral surface structure and the film registry. Figures 6–10 display LEED patterns for samples grown at different substrate temperatures and oxygen partial pressures, leading to varying ceria oxidation states and, consequently, different LEED patterns, which will be discussed in the following.

Before we present and analyze our findings, we provide a brief overview of the published LEED patterns of ceria on Ru(0001)

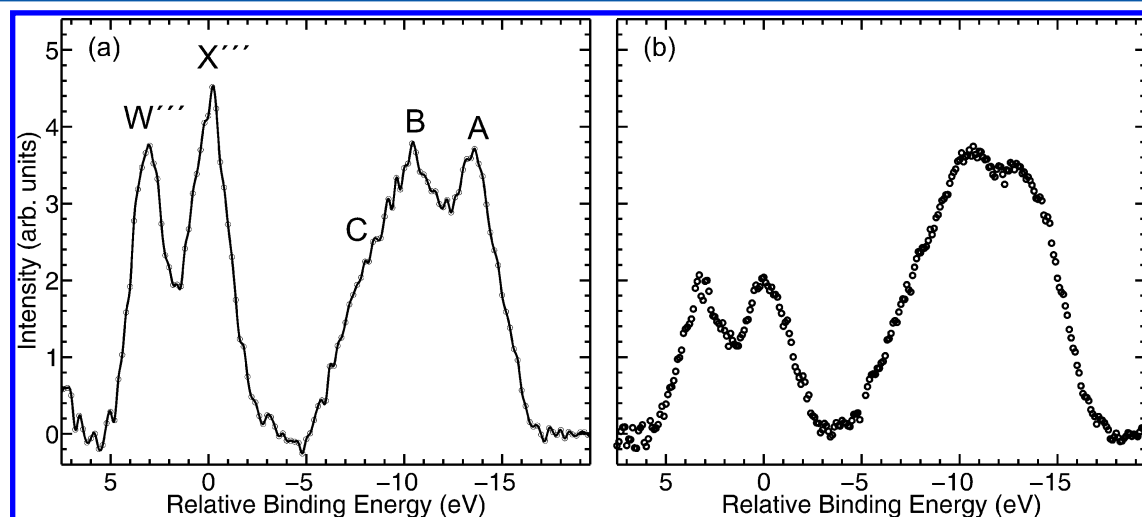


Figure 5. Ce 4d spectra after background subtraction of samples grown at 850 °C (a) and 360 °C (b) and oxygen partial pressures of 5×10^{-7} Torr (a) and 1×10^{-8} Torr (b) with ceria coverages of 5.6 ML (a) and 3.3 ML (b), respectively. The growth conditions for (a) lead to nearly fully oxidized ceria, whereas for (b), partially reduced ceria is observed.

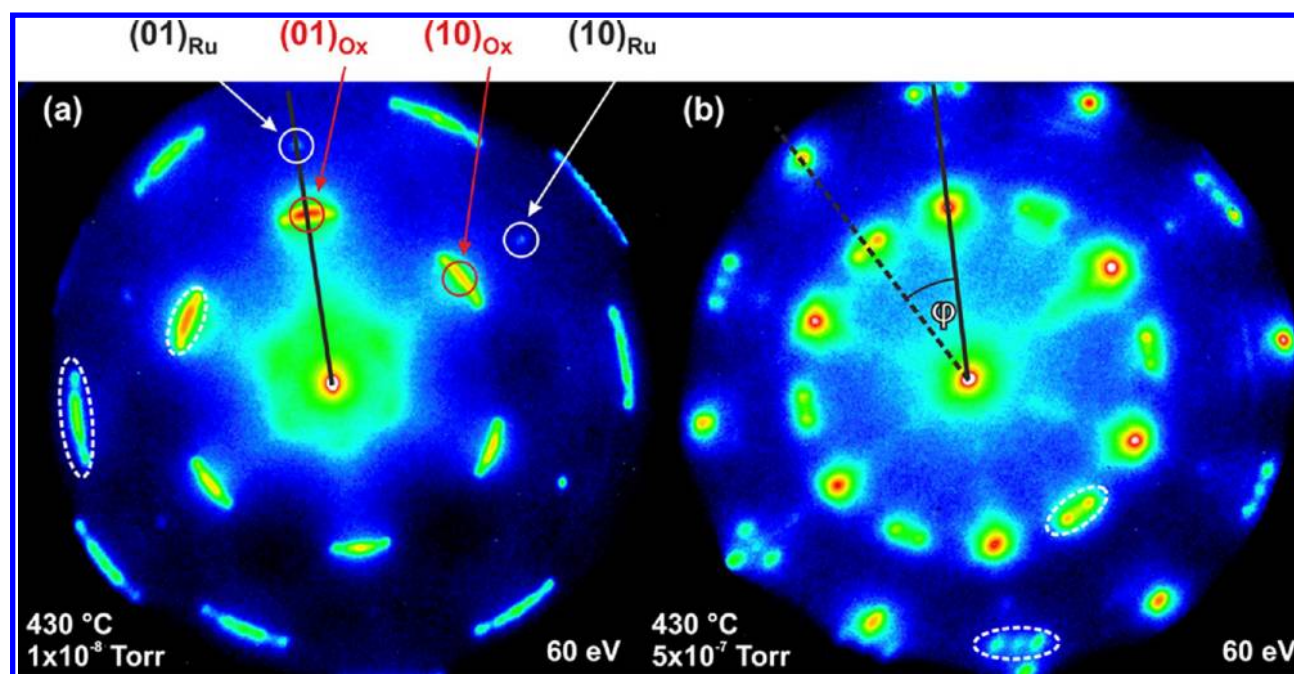


Figure 6. LEED images of 3 ML of ceria grown at a 430 °C substrate temperature and (a) an oxygen partial pressures of 1×10^{-8} Torr and (b) 5×10^{-7} Torr. Because of the difference in oxygen partial pressure during growth, (a) exhibits a very low oxidation state, whereas (b) is fully oxidized. The LEED images exhibit very faint Ru(0001) spots, indicating a not entirely covered substrate surface. The very intense diffraction spots belong to the $p(1.4 \times 1.4)$ ceria phase with additional rotational domains, which depend on the oxidation state of ceria. For a low oxidation state (a), the average direction of the B-type ceria rotational domains is in the substrate direction (black line), whereas it is rotated by $\varphi = 30^\circ$ (dashed black line) for fully oxidized ceria (b). The white dashed ellipses exemplarily highlight the different azimuthal intensity distributions for A- and B-type ceria rotational domains (a) and B-type ceria rotational domains (b) for the first- and second-order reflections.

and other transition-metal surfaces and how their occurrence can be rationalized based on a basic comparison of bulk crystal structures and their respective lattice constants. Depending on oxidation state, bulk cerium oxide crystallizes in different structures, which are associated with different surface lattice constants a_{surf} . For fully oxidized ceria (CeO_2 , fluorite structure), $a_{\text{surf}}^{\text{CeO}_2(111)} = 3.82 \text{ \AA}$, whereas $a_{\text{surf}}^{\text{Ce}_2\text{O}_3(111)} = 3.95 \text{ \AA}$ and $a_{\text{surf}}^{\text{Ce}_2\text{O}_3(0001)} = 3.89 \text{ \AA}$ have been reported for reduced ceria Ce_2O_3 in the bixbyite and hexagonal crystal phases, respectively.¹ For reference, the surface lattice constant of Ru(0001) is $a_{\text{surf}}^{\text{Ru}(0001)} = 2.706 \text{ \AA}$. Therefore, in the simplest approximation, an incoherent superposition of 3- or 6-fold symmetric LEED patterns is expected, with the respective cerium oxide diffraction spots located closer to the specular (00) reflection by a factor of about 1.41–1.46 than the integral order beams of the Ru reference lattice. If the two lattices are aligned with respect to the principal crystallographic axes, this is denoted as $p(1.41 \times 1.41)$ or $p(1.46 \times 1.46)$, respectively. Such a $p(1.4 \times 1.4)$ LEED pattern has been reported previously for fully oxidized $\text{CeO}_2(111)/\text{Ru}(0001)$.^{12,15}

This concept can also be transferred to the situation when ceria is grown on transition-metal substrates other than Ru(0001) with differently sized, but symmetry-wise identical two-dimensional unit meshes, for example, Rh(111) ($a_{\text{Rh}(111)} = 2.69 \text{ \AA}$) or Cu(111) ($a_{\text{Cu}(111)} = 2.55 \text{ \AA}$), for which $p(1.4 \times 1.4)$ ¹⁴ and $p(1.5 \times 1.5)$ ¹¹ LEED patterns have been observed. In the latter case, it was speculated by the same authors that the ceria layer could be commensurate since $3a_{\text{Cu}(111)} \approx 2a_{\text{CeO}_2(111)}$; however, no experimental evidence was presented.

In our LEED investigations, we will first elucidate the influence of the oxidation state of ceria on the structure (which is reflected by the LEED pattern, of course). Second, we will discuss the

$p(1.4 \times 1.4)$ diffraction pattern from ceria on Ru(0001) and the formation of rotational domains depending on growth temperature. For convenience, we here define two types of rotational domains. In the following, we define type A rotational domains as cerium oxide patches whose principal azimuthal directions are perfectly aligned with the substrate lattice, whereas type B rotational domains include all other domains that exhibit a nonvanishing angle $\varphi \neq 0$, as shown in Figure 6b. Furthermore, we will illustrate the formation of the well-known Ru(0001)- $p(2 \times 2)\text{O}$ phase,⁴⁴ which shows antiphase domain boundaries at certain growth conditions, revealing the presence of small oxygen domains on the Ru(0001) surface. Finally, we will unravel the origin of the $p(1.4 \times 1.4)$ LEED pattern of ceria on Ru(0001). By using the high resolution and sensitivity of the Elmitec SPE-LEEM instrument, we will show that the $p(1.4 \times 1.4)$ LEED pattern consists of an incoherent superposition of a (7×7) superstructure and the (1×1) diffraction spots of $\text{CeO}_x(111)$ islands, which coincide with the $(5/7)$ spots of a commensurate (7×7) superstructure.

To start off the discussion, 3 ML of ceria was deposited at 430 °C and an oxygen partial pressure of 1×10^{-8} Torr, leading to very small ceria islands with a very high density and a comparatively low oxidation state. The corresponding LEED image taken at 60 eV is shown in Figure 6a. The LEED pattern clearly shows the $p(1.4 \times 1.4)$ structure of ceria on Ru(0001), with strongly attenuated substrate spots, demonstrating an almost entirely continuous ceria film. In addition, B-type domains are visible, which are rotated by up to $\pm 10^\circ$, as evidenced by the azimuthal smearing of the ceria LEED spots. The average alignment of these B-type domains is along the azimuthal directions of the reciprocal lattice of the substrate; that is, the average angle $\langle \varphi \rangle = 0$, as highlighted by the black line in

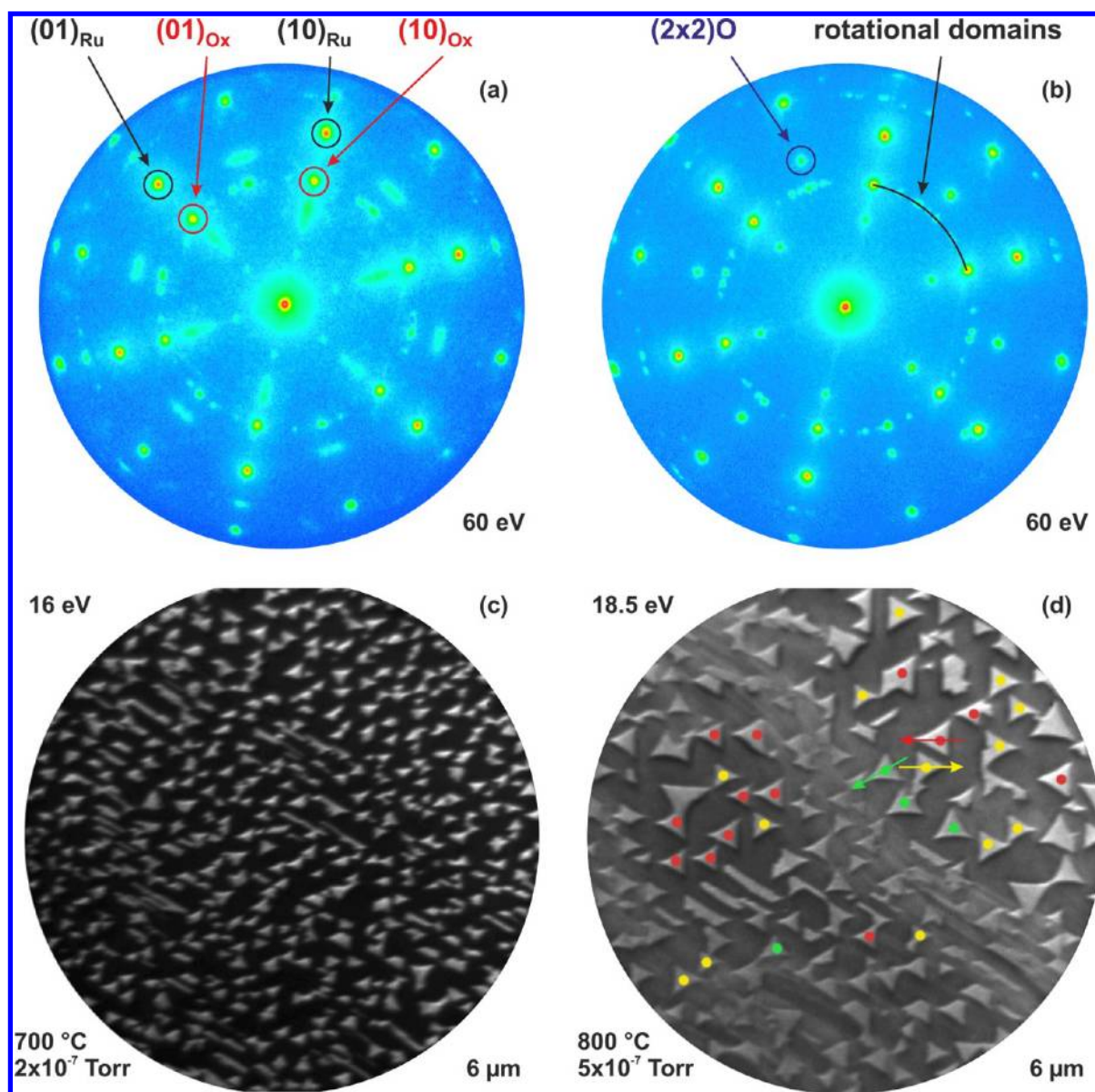


Figure 7. LEED and LEEM images of highly oxidized ceria grown at (a) a 700 °C substrate temperature and an oxygen partial pressure of 2×10^{-7} Torr and (b) an 800 °C substrate temperature and an oxygen partial pressure of 5×10^{-7} Torr. Both LEED patterns exhibit the Ru(0001) substrate spots and the $p(1.4 \times 1.4)$ ceria phase with additional rotational domains. The average direction of the ceria B-type rotational domains is rotated by 30° with respect to principal azimuthal directions of the substrate. The number of rotational domains is higher for pattern (b). Also, the $p(2 \times 2)$ O phase is observed in both LEED patterns with an additional splitting of the spots in pattern (a), which can be attributed to antiphase domain boundaries with a respective domain size of 3.2 ± 0.2 nm. Pattern (b) does not exhibit a splitting of the $p(2 \times 2)$ O phase. Panels (c) and (d) are the LEEM images corresponding to (a) and (b), respectively. In panel (d), characteristic ceria islands are highlighted by different colors. The red and yellow marked islands are rotated by 180° with respect to each other, whereas the green labeled islands are rotated by 30° with respect to the red islands.

Figure 6a. Their intensity distribution $I(\varphi)$ appears to be Gaussian-like, which is exemplarily marked by the inner white dashed ellipse in Figure 6a for the first-order reflections. For the second-order reflections, however, discrete spots are observed, which are again exemplarily highlighted by the outer dashed ellipse and are best visible at the ends of the dashed ellipse, corroborating the presence of well-ordered islands exhibiting varying azimuthal orientations.

When we increase the oxidation state of ceria to fully oxidized ceria by deposition at higher oxygen partial pressure, the LEED pattern, and, specifically, the azimuthal distribution of the rotational domains, changes dramatically. A respective LEED image is shown in Figure 6b for 3 ML of ceria deposited at 430°

and an oxygen partial pressure of 5×10^{-7} Torr. Again, the $p(1.4 \times 1.4)$ LEED pattern along with very faint Ru(0001) spots is clearly visible, illustrating ordered A-type ceria domains and a highly covered Ru(0001) surface, respectively. However, the most obvious change in the LEED pattern is due to the B-type ceria domains, whose average rotation amounts to $\langle \varphi \rangle = 30^\circ$, as indicated by the dashed black line and the angle φ in Figure 6b. Also, the number of rotational domains is decreased, as can be inferred from the decrease in intensity as compared to the A-type domains. We also note that, in Figure 6b, mainly three distinct B-type domains are visible, essentially suggesting a trimodal distribution $I(\varphi)$ for the B-type ceria domains, in stark contrast to

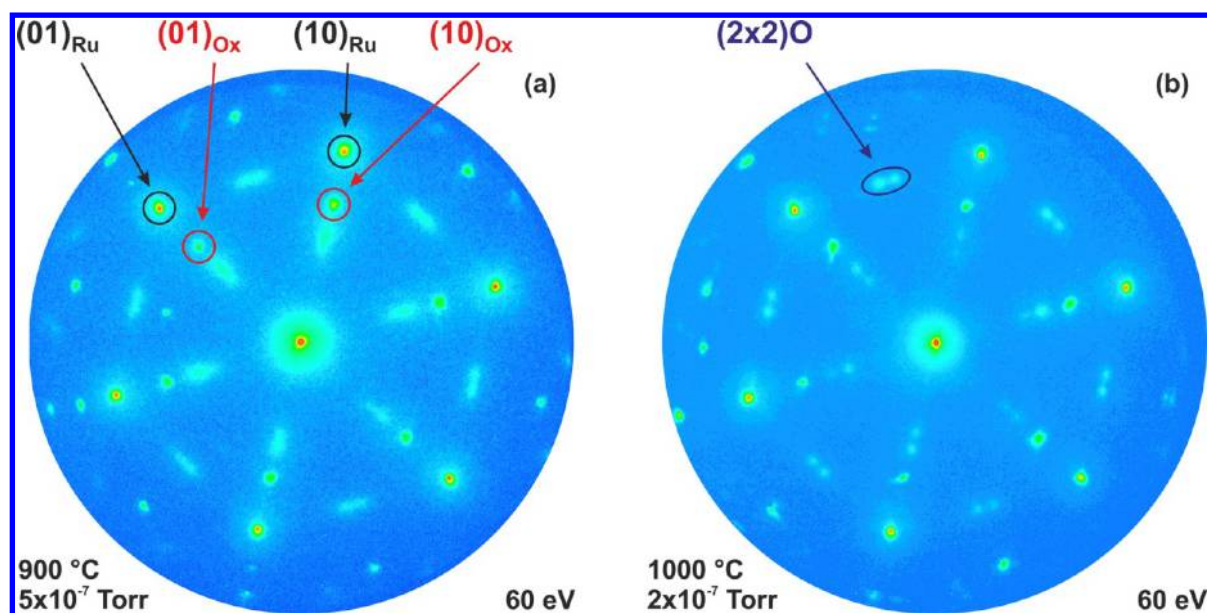


Figure 8. LEED images of highly oxidized ceria grown at (a) a 900 °C substrate temperature and an oxygen partial pressure of 5×10^{-7} Torr and (b) a 1000 °C substrate temperature and an oxygen partial pressure of 5×10^{-7} Torr. Both LEED patterns exhibit the Ru(0001) substrate spots and the $p(1.4 \times 1.4)$ ceria phase. The $p(2 \times 2)$ O phase is observed in both LEED patterns with an additional splitting of the spots, which can be attributed to antiphase domain boundaries with a respective domain size of 3.2 ± 0.2 nm.

reduced ceria, which exhibits a Gaussian-type distribution (Figure 6a).

Thus, we conclude that, for a low oxidation state, the average direction of the B-type ceria domains is aligned with the principal azimuthal directions of the substrate, whereas for fully oxidized ceria, the average direction of the B-type domains deviates by 30° (Figure 6b). Also, the number of B-type domains obtained at a growth temperature of 430 °C is significantly decreased with an increase in oxidation state. The mere existence of ceria rotational domains has already been reported previously by Lu et al.,¹⁵ who, using STM, presented evidence for ceria domains rotated by 30° relative to each other. In the same study, different types of rotational domains were also visible in LEED; however, their occurrence and type were not correlated with growth temperature and ceria oxidation state.

To investigate the influence of growth temperature on the lateral film structure of highly oxidized ceria on Ru(0001), we will now discuss the LEED patterns of samples grown in the temperature regime between 700 and 1000 °C. The oxygen partial pressure applied during growth was 2×10^{-7} Torr for a sample grown at 700° and 5×10^{-7} Torr for all other samples, ensuring a high oxidation state of ceria. The respective LEED images are shown in Figures 7 and 8. In both figures, and also in Figure 10, the Ru(0001) diffraction spots exhibit a very high intensity, which corroborates the presence of a discontinuous film. This is expected for ceria coverages up to 4.5 ML since ceria on Ru(0001) adheres to a Volmer–Weber growth mode, with the island nucleation density decreasing and the average island size increasing with growth temperature. The $p(1.4 \times 1.4)$ LEED pattern is observed for all temperatures between 700 and 1000 °C. However, both the azimuthal distribution of the B-type domains and their relative fraction are seen to strongly depend on growth temperature. The average angle between the ceria B-type rotational domains and the reciprocal lattice of the substrate is $\langle \varphi \rangle = 30^\circ$ for all four samples, while the number of B-type domains has its maximum at an 800 °C growth temperature and decreases for lower and higher deposition temperatures. At a 900

°C growth temperature, only one B-type domain is observed, whereas at a deposition temperature of 1000 °C, no B-type domains are present anymore.

For the LEED images shown in panels (a) and (b) in Figure 7, panels (c) and (d) in Figure 7 show the respective real-space images at an FOV of 6 μm . Representative ceria islands are illustrated in real space with different colors for the sample grown at 800 °C in Figure 7d. The red and yellow marked islands are rotated by 180° with respect to each other and, therefore, cannot be distinguished in the LEED pattern. The islands highlighted by the green points are rotated by 30° with respect to the red ones and also appear with a rotation angle of $\varphi = 30^\circ$ in the LEED pattern. Because we observe mainly red and yellow marked islands in the real-space image, they contribute the highest intensity to the ceria spots in the LEED pattern. Therefore, by comparison with the intensity distribution of the ceria diffraction spots, we conclude that the crystal lattices of these ceria islands and the substrate are aligned to each other; that is, the red and yellow dots mark the A-type ceria domains. Because most of the large, well-aligned, almost perfectly triangular ceria islands are located on the substrate terraces in Figure 7d, we conclude that the red, yellow, and green ceria islands preferentially develop on the substrate terraces or at atomic steps. Because the LEED pattern in Figure 7b also exhibits B-type ceria domains with an azimuthal orientation $\varphi \neq 30^\circ$, which cannot be found on the substrate terraces in the real-space image, we suggest that these ceria islands primarily nucleate at the substrate step bunches. Again, this finding illustrates the influence of the substrate on the growth and morphology of the ceria islands.

The LEED patterns of the samples grown between 700 and 1000 °C also exhibit the $p(2 \times 2)$ O phase.⁴⁷ In Figures 7a and 8a,b, the $p(2 \times 2)$ O phase clearly shows an additional splitting of the diffraction spots, which can be attributed to antiphase domain boundaries. From the splitting, we deduce an average $p(2 \times 2)$ O domain size of 3.2 ± 0.2 nm, which does not change with temperature within the error bar. The sample grown at 800 °C

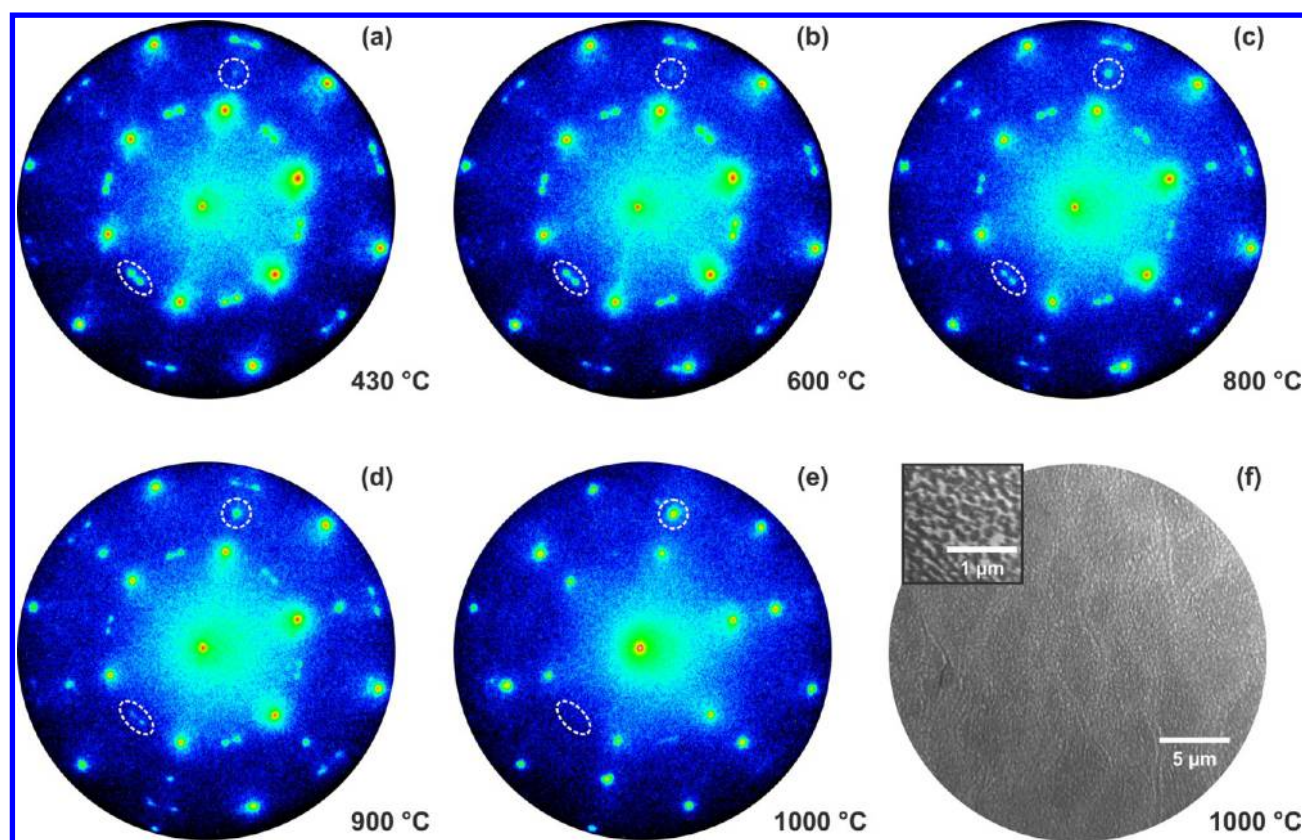


Figure 9. Series of single-frame LEED images (a)–(e) acquired at an electron energy of 60 eV during annealing of 2.4 ML of fully oxidized ceria grown at a 430 °C substrate temperature and an oxygen partial pressure of 2×10^{-7} Torr. The annealing was performed with no oxygen background applied up to 1000 °C (e). Panel (a) shows a typical LEED image of fully oxidized ceria grown at 430 °C with its characteristic distribution of A- and B-type ceria domains. With increasing temperature ((b)–(e)), the intensity of the B-type domains decreases while the intensity of A-type domains relative to the B-type domains increases. Furthermore, the ruthenium diffraction spots gain in intensity with increasing temperature. At 1000 °C, no B-type domains are visible anymore. The white dashed ellipse and the white dashed circle exemplarily highlight the B-type ceria domains and the ruthenium diffraction spots for the first-order reflection in the annealing sequence (a)–(e), respectively. Panel (f) shows a real-space LEEM image acquired at a kinetic electron energy of 21.9 eV after annealing up to 1000 °C in 3×10^{-7} Torr oxygen backfilling. The inset shows an image acquired at higher resolution and an electron energy of 22.5 eV, illustrating the formation of irregular patches upon annealing.

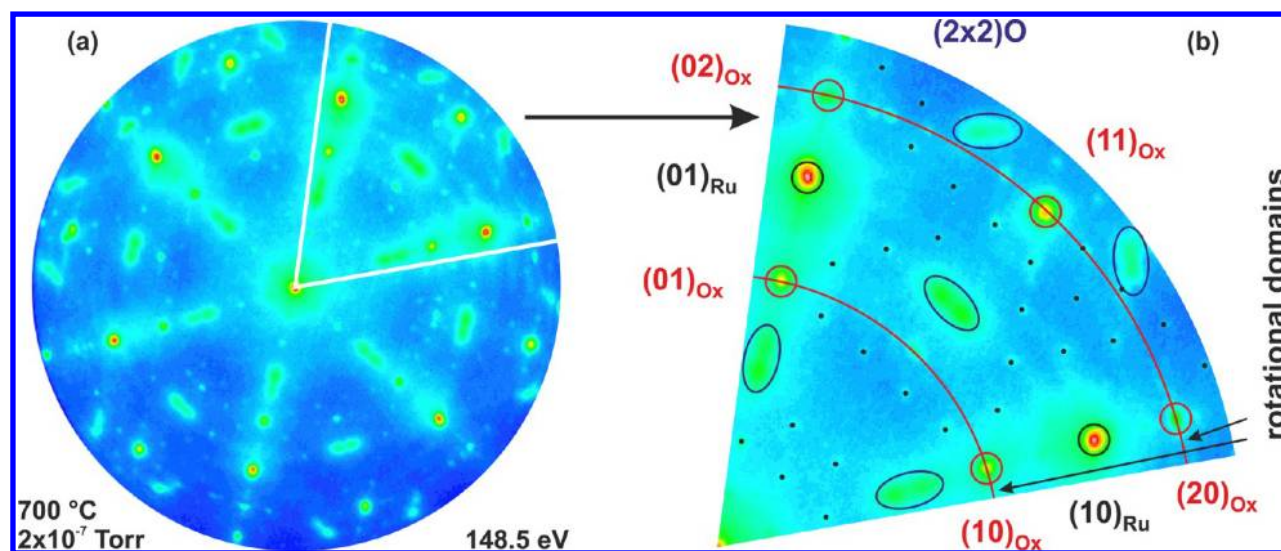


Figure 10. LEED image of highly oxidized ceria grown at a 700 °C substrate temperature and an oxygen partial pressure of 2×10^{-7} Torr. Panel (b) shows a magnified part of the LEED pattern. All main diffraction spots are labeled in (b) by different colored circles or ellipses. The LEED pattern exhibits the Ru(0001) substrate spots and the $p(1.4 \times 1.4)$ ceria phase with an additional (7×7) superstructure, which is highlighted by the small black dots. Also, the $p(2 \times 2)O$ phase is observed with an additional splitting of the diffraction spots, which can be attributed to antiphase domain boundaries with a respective domain size of 3.2 ± 0.2 nm. The thin red circular lines highlight possible positions for ceria rotational domains.

does not show a splitting of the $p(2 \times 2)\text{O}$ diffraction spots and, therefore, does not exhibit antiphase domain boundaries.

For all the growth conditions discussed above, we investigated the reciprocal space with electron energies in the range between 40 and 100 eV (data not shown). In all of these studies, we did not observe any facets. This is why we conclude that ceria islands under the growth conditions used in our experiments do not develop extended facets. This finding is in agreement with our AFM results.

To study the behavior of A- and B-type ceria domains during high-temperature annealing, we present a series of single-frame LEED images in Figure 9a–e that were recorded for 2.4 ML of ceria grown at 430 °C and 2×10^{-7} Torr oxygen partial pressure during annealing up to 1000 °C with no oxygen backfilling applied. Figure 9a shows a typical LEED pattern of fully oxidized ceria grown at 430 °C with the characteristic distribution of A- and B-type ceria domains. As the temperature is increased up to 1000 °C, the intensity of the B-type domains relative to the A-type domains decreases while the ruthenium (1×1) diffraction spots become more pronounced. At a 1000 °C substrate temperature (Figure 9e), the ruthenium diffraction spots account for the highest intensity in the LEED image, and only A-type ceria domains are visible anymore, whereas all B-type domains have disappeared. This means that the amount of B-type ceria domains can be decreased by high-temperature annealing at the expense of a continuous ceria film. Interestingly, the same correlation is observed for an annealing sequence in 3×10^{-7} Torr oxygen backfilling (data not shown). Therefore, we conclude that the oxygen partial pressure during annealing has no influence on the relative stability of A- and B-type ceria domains. We also note that we did not observe any $p(2 \times 2)\text{O}$ phase in LEED during annealing, which is in stark contrast to the growth at elevated temperatures discussed before.

A representative real-space image of the ceria film recorded after annealing to 1000 °C under oxygen backfilling is shown in Figure 9f. Apparently, the morphology of the annealed ceria film is completely different from the morphology of ceria grown at high temperatures. Here, instead of large, almost perfectly triangular islands, irregularly shaped ceria patches are observed.

In all of our LEED investigations, we could clearly see $p(1.4 \times 1.4)$ spots, which are attributed to ceria. To get an even more detailed insight into reciprocal space and to reveal the origin of the $p(1.4 \times 1.4)$ phase, that is, whether it is a commensurate or an incommensurate phase, we recorded a LEED image of the sample grown at 700 °C and a kinetic energy of 148.5 eV, which is shown in Figure 10a. For an improved visibility, a magnified view of the region enclosed by white lines in Figure 10a is displayed in Figure 10b. As expected, the LEED pattern exhibits the Ru(0001) diffraction spots (black circles) as well as the well-known $p(1.4 \times 1.4)$ ceria spots (red circles). Also, the $p(2 \times 2)\text{O}$ phase with an additional splitting due to antiphase domain boundaries is visible (blue ellipse). Diffraction spots belonging to ceria rotational domains occur at positions that are highlighted by red circular lines. All of these findings could already be observed in the LEED pattern recorded at 60 eV in Figure 7. The really new and exciting finding from Figure 10 are the small $(n/7)$ spots, whose positions are marked by small black dots. These diffraction peaks could be observed for the first time, probably owing to the superior resolution and sensitivity of the SPE-LEEM instrument as compared to a conventional LEED system. Since the $(n/7)$ spots all exhibit comparable intensity, we do not observe the characteristic, damped envelope function typical of a moiré pattern, which would be representative of a coincidence

lattice for ceria on Ru(0001). This observation clearly reveals that ceria on Ru(0001) develops a (7×7) superstructure and is, therefore, commensurate. The $(5/7)$ spots exhibit the highest intensity because they coincide with the (1×1) diffraction spots of bulk $\text{CeO}_{2-\delta}(111)$. The LEED pattern can, therefore, be explained by a superposition of the diffraction from $\text{CeO}_{2-\delta}(111)$ -type islands and from regions where the islands are sufficiently thin so that we can still probe the (7×7) superstructure at the interface. Furthermore, the moderate increase in electron energy by a factor of about 2.5 may also be partly responsible for the slightly diminished attenuation and hence enhanced sensitivity to the oxide–metal interface.

Summarizing the LEED analysis, the overall picture emerges that ceria on ruthenium (0001) forms a commensurate (7×7) superstructure, which implies that the atomic interface between the ceria islands and the ruthenium substrate is well-ordered and coherent. For other ceria inverse catalyst model systems, for example, ceria on $\text{Pt}(111)$ ⁴² and ceria on $\text{Rh}(111)$,¹⁴ such a commensurate ceria superstructure has not been reported yet. We suggest that this difference may be due to an increased tendency for substrate oxidation and intermixing reported for other transition-metal substrates.^{14,37,42}

CONCLUSION

Using a combination of low-energy electron microscopy and diffraction, X-ray photoemission spectroscopy, and atomic force microscopy on the same set of samples, we studied the growth and structural properties of cerium oxide on Ru(0001) under varying preparation conditions. Specifically, we could infer that ceria adopts a Volmer–Weber growth mode, resulting in the evolution of single-crystalline 3D islands, whose size and nucleation density strongly depend on deposition temperature and surface morphology: First, with increasing temperature, the island size increases while the nucleation density decreases in an Arrhenius-like behavior. Second, the island density is significantly increased at step bunches, whereas, at the ruthenium terraces, the islands preferentially develop a nonequilateral, but otherwise perfectly triangular, shape. Furthermore, the ceria island edges are very sharp and steep; thus, no distinct side facets could be observed. Especially for high growth temperatures, the (111) top facets become very smooth and highly ordered and typically exhibit very large terraces with only few monolayer steps on a micrometer scale, yielding even larger island terrace-to-step edge ratios than previously achieved for deposition at lower temperature, followed by postdeposition annealing.^{15,16}

We also demonstrated the strong influence of deposition temperature and oxidation state on the occurrence and orientation of $\text{CeO}_x(111)$ rotational domains, which we have classified into two distinct groups depending on their azimuthal alignment with respect to the main symmetry directions of the substrate. Interestingly, the azimuthal distribution and density of ceria rotational domains significantly differs for reduced and highly oxidized ceria. Moreover, the amount of low-symmetry rotational domains of highly oxidized ceria as a function of deposition temperature does not exhibit a monotonic behavior. It has its maximum at 800 °C and decreases for lower and higher temperatures.

Owing to the high resolution and sensitivity of the SPE-LEEM instrument in diffraction mode, the well-known $p(1.4 \times 1.4)$ phase could be “reinterpreted” as an incoherent superposition of an interfacial (7×7) superstructure and the (1×1) diffraction of the $\text{CeO}_{2-\delta}(111)$ ($\delta \ll 0.5$) islands. This finding reveals that ceria on ruthenium indeed forms a commensurate phase and that

the interface between the oxide and the metal substrate is well-ordered. This is the first time that a true superstructure at the oxide–metal interface is reported for a ceria-containing inverse catalyst model system.

In more general terms, our results show that, by selecting appropriate growth conditions (temperature, oxygen partial pressure), the ceria island size and nucleation density as well as the number, type, and shape of the ceria rotational domains can be controlled. These findings should have significant implications for both fundamental and more applied studies using cerium oxide as catalyst material: On one hand, the enhanced understanding of the dependence of the surface structure on the preparation conditions will help in designing even better-defined ceria inverse model catalysts, allowing one to more clearly isolate and identify the basic structure–function relationships in distinct surface-chemical reactions. On the other hand, an enhanced structural control of the ceria catalyst could also have a tremendous impact on the ability to tailor the reactivity of the ceria on the Ru(0001) system since surface oxygen vacancies, and surface defects, for example, step edges, in general, are considered catalytically very active sites. By being able to control the number, type, and alignment of rotational domains, it could very well be possible not only to increase the total number of defects but also to control their specific nature, for example, the actual type of step edges, and, therefore, fine-tune the chemical properties of the catalyst material. Furthermore, our first in situ results reported for the high-temperature behavior of cerium oxide are expected to have important implications for the use of ceria-based catalysts under extreme conditions, for example, those found in solar reactor chemistry.⁴⁶

AUTHOR INFORMATION

Corresponding Author

*E-mail: flege@ifp.uni-bremen.de.

Notes

The authors declare no competing financial interest.

ACKNOWLEDGMENTS

The authors would like to thank Percy Zahl, Peter Sutter (Center for Functional Nanomaterials, BNL), Gary Nintzel (National Synchrotron Light Source, BNL), and Jürgen Lauckner (Universität Bremen) for technical support. Research was carried out, in part, at the Center for Functional Nanomaterials and the National Synchrotron Light Source, Brookhaven National Laboratory, which is supported by the U.S. Department of Energy, Office of Basic Energy Sciences, under Contract No. DE-AC02-98CH10886.

REFERENCES

- (1) Trovarelli, A., Ed. *Catalysis by Ceria and Related Materials*; Imperial College Press: London, 2002.
- (2) Steele, B. C. H.; Heinzl, A. *Nature* **2001**, *414*, 345–352.
- (3) Wang, Y.; Wei, F.; Yue, S.; Yang, Z.; Du, J. *Appl. Phys. Lett.* **2008**, *92*, 012915.
- (4) Chen, C.-H.; Chang, I. Y.-K.; Lee, J. Y.-M.; Chiu, F.-C. *Appl. Phys. Lett.* **2008**, *92*, 043507.
- (5) Chikyow, T.; Bedair, S. M.; Tye, L.; El-Masry, N. A. *Appl. Phys. Lett.* **1994**, *65*, 1030–1032.
- (6) Rodriguez, J. A.; Ma, S.; Liu, P.; Hrbek, J.; Evans, J.; Pérez, M. *Science* **2007**, *318*, 1757–1760.
- (7) Chueh, W. C.; Falter, C.; Abbott, M.; Scipio, D.; Furler, P.; Haile, S. M.; Steinfeld, A. *Science* **2010**, *330*, 1797–1801.
- (8) Mullins, D. R. *J. Electron Spectrosc. Relat. Phenom.* **2001**, *114*–116, 333–337.
- (9) Idriss, H.; et al. *ChemSusChem* **2008**, *1*, 905–910.
- (10) Ma, S.; Rodriguez, J.; Hrbek, J. *Surf. Sci.* **2008**, *602*, 3272–3278.
- (11) Matolín, V.; Libra, L.; Matolínová, I.; Nehasil, V.; Sedláček, L.; Šutara, F. *Appl. Surf. Sci.* **2007**, *254*, 153–155.
- (12) Mullins, D. R.; Radulovic, P. V.; Overbury, S. H. *Surf. Sci.* **1999**, *429*, 186–198.
- (13) Xiao, W.; Guo, Q.; Wang, E. G. *Chem. Phys. Lett.* **2003**, *368*, 527–531.
- (14) Eck, S.; Castellarin-Cudia, C.; Surnev, S.; Ramsey, M. G.; Netzer, F. P. *Surf. Sci.* **2002**, *520*, 173–185.
- (15) Lu, J.-L.; Gao, H.-J.; Shaikhutdinov, S.; Freund, H.-J. *Surf. Sci.* **2006**, *600*, 5004–5010.
- (16) Zhou, J.; Baddorf, A. P.; Mullins, D. R.; Overbury, S. H. *J. Phys. Chem. C* **2008**, *112*, 9336–9345.
- (17) Škoda, M.; Libra, J.; Šutara, F.; Tsud, N.; Skála, T.; Sedláček, L.; Prince, K. C.; Cháb, V.; Matolín, V. *Surf. Sci.* **2007**, *601*, 4958–4965.
- (18) Berner, U.; Schierbaum, K.-D. *Phys. Rev. B* **2002**, *65*, 235404.
- (19) Putna, E. S.; Vohs, J. M.; Gorte, R. J. *J. Phys. Chem. C* **1996**, *100*, 17862–17865.
- (20) Putna, E. S.; Bunluesin, T.; Fan, X. L.; Gorte, R. J.; Vohs, J. M.; Lakis, R. E.; Egami, T. *Catal. Today* **1999**, *50*, 343–352.
- (21) Kundakov, L.; Mullins, D. R.; Overbury, S. H. *Surf. Sci.* **2000**, *457*, 51–62.
- (22) Overbury, S. H.; Mullins, D. R.; Huntley, D. R.; Kundakov, L. *J. Phys. Chem. B* **1999**, *103*, 11308–11317.
- (23) Mullins, D. R.; Senanayake, S. D.; Chen, T.-L. *J. Phys. Chem. C* **2010**, *114*, 17112–17119.
- (24) Chen, T.-L.; Mullins, D. R. *J. Phys. Chem. C* **2011**, *115*, 13725–13733.
- (25) Nilius, N.; Kozlov, S. M.; Jerratsch, J.-F.; Baron, M.; Shao, X.; Viñes, F.; Shaikhutdinov, S.; Neyman, K. M.; Freund, H.-J. *ACS Nano* **2012**, *6*, 1126–1133.
- (26) Esch, F.; Fabris, S.; Zhou, L.; Montini, T.; Africh, C.; Fornasiero, P.; Comelli, G.; Rosei, R. *Science* **2005**, *309*, 752–755.
- (27) Shao, X.; Jerratsch, J.-F.; Nilius, N.; Freund, H.-J. *Phys. Chem. Chem. Phys.* **2011**, *13*, 12646–12651.
- (28) Torbrügge, S.; Reichling, M.; Ishiyama, A.; Morita, S.; Custance, O. *Phys. Rev. Lett.* **2007**, *99*, 056101.
- (29) Flege, J. I.; Vescovo, E.; Nintzel, G.; Lewis, L. H.; Hulbert, S.; Sutter, P. *Nucl. Instrum. Methods Phys. Res., Sect. B* **2007**, *261*, 855–858.
- (30) Madey, T. E.; Engelhardt, H. A.; Menzel, D. *Surf. Sci.* **1975**, *48*, 304–328.
- (31) Zahl, P.; Wagner, T.; Möller, R.; Klust, A. *J. Vac. Sci. Technol., B* **2010**, *28*, C4E39–C4E47.
- (32) Over, H.; Muhler, M. *Prog. Surf. Sci.* **2003**, *72*, 3–17.
- (33) Flege, J. I.; Hrbek, J.; Sutter, P. *Phys. Rev. B* **2008**, *78*, 165407.
- (34) Flege, J. I.; Sutter, P. *J. Phys.: Condens. Matter* **2009**, *21*, 314018.
- (35) Venables, J. A.; Spiller, G. D. T.; Hanbücken, M. *Rep. Prog. Phys.* **1984**, *47*, 399–459.
- (36) Bauer, E. Z. *Kristallogr.* **1958**, *110*, 372–394.
- (37) Luches, P.; Pagliuca, F.; Valeri, S. *J. Phys. Chem. C* **2011**, *115*, 10718–10726.
- (38) Castellarin-Cudia, C.; Surnev, S.; Schneider, G.; Podlicky, R.; Ramsey, M. G.; Netzer, F. P. *Surf. Sci.* **2004**, *554*, L120–L126.
- (39) Kotani, A.; Ogasawara, H. *J. Electron Spectrosc. Relat. Phenom.* **1992**, *60*, 257–299.
- (40) Mullins, D. R.; Overbury, S. H.; Huntley, D. R. *Surf. Sci.* **1998**, *409*, 307–319.
- (41) Baron, M.; Bondarchuk, O.; Stacchiola, D.; Shaikhutdinov, S.; Freund, H.-J. *J. Phys. Chem. C* **2009**, *113*, 6042–6049.
- (42) Schierbaum, K.-D. *Surf. Sci.* **1998**, *399*, 29–38.
- (43) Matolín, V.; Matolínová, I.; Sedláček, L.; Prince, K. C.; Skála, T. *Nanotechnology* **2009**, *20*, 215706.
- (44) Grant, J. T.; Haas, T. W. *Surf. Sci.* **1970**, *21*, 76–85.
- (45) Kostov, K. L.; Gsell, M.; Jakob, P.; Moritz, T.; Widdra, W.; Menzel, D. *Surf. Sci.* **1997**, *394*, L138–L144.
- (46) Furler, P.; Scheffe, J. R.; Steinfeld, A. *Energy Environ. Sci.* **2012**, *5*, 6098–6103.

(47) At this point, we cannot exclude the presence of the $p(2 \times 2)3\text{O}$ phase⁴⁵ based on LEED. However, considering the high temperatures used, we regard this interpretation as unlikely.